

# Cavity-Waveguide Coupling Engineered High Sensitivity Silicon Photonic Crystal Microcavity Biosensors With High Yield

Yi Zou, Swapnajit Chakravarty, *Senior Member, IEEE*, David N. Kwong, Wei-Cheng Lai, Xiaochuan Xu, Xiaohui Lin, Amir Hosseini, *Member, IEEE*, and Ray T. Chen, *Fellow, IEEE*

**Abstract**—We present a high yield and high sensitivity on-chip biosensing system by combining subwavelength grating coupling and high sensitivity photonic crystal microcavity side coupled to a photonic crystal waveguide. 80% yield of working devices was experimentally demonstrated for sensitivity engineered L13 photonic crystal microcavities and 70% for L21 photonic crystal microcavities. Subwavelength grating couplers significantly improved the quality of the output transmission spectrum. By engineering the optical loss rate from the cavity to the waveguide, we experimentally detected 1 pM (67 pg/ml) and 50 femto-molar (3.35 pg/ml) concentration of avidin binding to biotin in phosphate buffered saline for L21 and L55 PC microcavities respectively, which represents the highest sensitivity versus other chip-based optical biosensors.

**Index Terms**—Photonic crystals, photonic crystal waveguides, photonic integrated circuits, sensors.

## I. INTRODUCTION

SILICON photonics is a promising platform for high density integration of photonic devices. Since it is compatible with CMOS fabrication, hence high volume manufacturing is feasible. However, although silicon photonics has several performance advantages, coupling of light into and out of silicon devices reliably has been a primary impediment towards large scale adoption to real applications. Optical fibers are the primary medium for guiding light into and out of the photonic chips. However, silicon based optical devices suffer very high loss when coupling light into/out from chips, due to large mode and effective index mismatches between fiber and silicon waveguide, dimensions of which are of the order of several hundred nanometers. Several coupling approaches have been proposed to address this problem. Methods typically adopted are

inverse tapers [1]–[4] and grating couplers which include traditional air trench grating design [5]–[10] and subwavelength nanostructures [11]–[16]. The results show that coupling efficiency can be significantly improved in subwavelength grating couplers which therefore provide significant design freedom to meet the requirement of different applications. In recent work, it was shown that subwavelength grating couplers with high coupling efficiency for transverse-electric (TE) polarization can be fabricated simultaneously with other photonic devices thereby adding no additional steps in fabrication [15]. In particular, a 2-D photonic crystal comprising air holes etched into dielectric silicon supports an in-plane band gap for light with TE polarization but does not support a sufficiently wide in-plane band gap for transverse-magnetic (TM) polarization. Consequently, a TE selective subwavelength grating coupler introduces an additional polarization filter that further increases the extinction ratio between TE and TM polarizations inside the photonic crystal waveguide. In recent years, photonic crystal (PC) microcavities, because of its compact size (of the order of a few square microns in surface area) and high sensitivity, have attracted significant interest in biosensing. The principle of operation transduces the specific binding of the biomolecule of interest to its conjugate biomolecule receptor bound to the photonic crystal microcavity into an optical signal. When compared to other chip-integrated sensing platforms such as ring-resonators [17], [18], wire waveguides [19] and surface plasmon resonance [20], PC microcavities have higher sensitivity due to its slow light effect, high quality factor resonances and a larger optical mode overlap with the analyte within a compact optical mode volume [21]. However, in spite of significant success in demonstrating highest sensitivity biosensors [22], working device yield using end-fire coupling, after successful fabrication was dismal, of the order of 10% in some instances [23].

In this letter, we show that by integrating subwavelength grating couplers with PC microcavity coupled waveguides for biosensing, coupling efficiency increased compared to previous end-fire coupling methods. Furthermore, the working device yield is significantly improved to 80% with significantly improved spectral purity of observed resonances. By further engineering the loss due to the leakage of light from the PC microcavity to the PC waveguide in addition to microcavity engineering to improve the uncoupled cavity quality factor, we experimentally detected biomolecular concentrations more than one order of magnitude better than our previous results [22]. Our preliminary yield results combining subwavelength grating

Manuscript received October 1, 2013; revised November 12, 2013; accepted November 12, 2013. This work was supported in part by the National Cancer Institute under Contract HHSN 261201200043C and in part by AFOSR MURI under Contract FA9550-08-1-0394.

Y. Zou, D. N. Kwong, W.-C. Lai, X. Xu, X. Lin, and R. T. Chen are with the Microelectronics Research Center, Department of Electrical and Computer Engineering, University of Texas, Austin, TX 78758 USA (e-mail: yzou@utexas.edu; david.kwong@utexas.edu; wlai@utexas.edu; xiaochuan.xu@utexas.edu; xiaohui.lin@utexas.edu; raychen@uts.cc.utexas.edu).

S. Chakravarty, and A. Hosseini are with the Omega Optics, Inc., Austin, TX 78759 USA (e-mail: swapnajit.chakravarty@omegaoptics.com; amirh@utexas.edu).

Color versions of one or more of the figures in this paper are available online at <http://ieeexplore.ieee.org>.

Digital Object Identifier 10.1109/JSTQE.2013.2291443

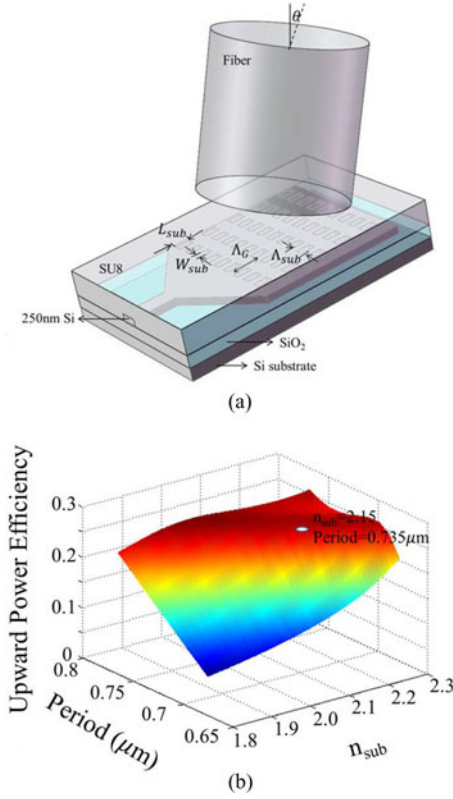


Fig. 1. (a) A schematic of subwavelength grating coupler. (b) Upward power efficiency as a function of grating period  $\Lambda_G$  and the effective refractive index  $n_{\text{sub}}$  of the subwavelength structure.

couplers with PC microcavity coupled waveguides are extremely significant for biosensing microarray applications that will consider dense integration of multiple simultaneously interrogated sensors on chip [24].

## II. DEVICE DESIGN AND PRINCIPLES

### A. Device Principles of Subwavelength Grating Coupler

The subwavelength grating (SWG) coupler works on the same principle as the traditional grating coupler. However, the SWG replaces the air trenches with a subwavelength nanostructure, as shown in Fig. 1(a). According to effective medium theory [25], a composite medium comprising two different materials interleaved at the subwavelength scale can be treated approximately as a homogenous medium with an effective refractive index between these two materials. Based on these two working principles, the SWG coupler covered by SU8 resist protection layer was simulated by 2-D simulation package CAMFR using the design rules laid down previously [15]. The grating period and effective refractive index were scanned simultaneously to get the maximum upward coupling efficiency through the SWG. The simulation result is shown in Fig. 1(b).

When the grating period  $\Lambda_G$  (in the propagation direction) is fixed at 735 nm and the effective refractive index  $n_{\text{sub}}$  of subwavelength region is set as 2.15 which are indicated in Fig. 1(b), the upward coupling efficiency to air reaches its maximum at around 26% with an emitting angle of  $14^\circ$ . The duty cycle is 50%. 22 periods are chosen to make the grating region  $14 \mu\text{m}$

wide and  $16 \mu\text{m}$  long that can match well with the mode size of a single mode fiber. The SWG size thus provides some tolerances to make the alignment easily during measurement [11].  $L_{\text{sub}}$  and  $W_{\text{sub}}$  represent the trench dimension along and perpendicular to the propagation direction respectively.  $\Lambda_{\text{sub}}$  is the grating period perpendicular to the propagation direction. The values for parameters  $\Lambda_{\text{sub}}$  and  $W_{\text{sub}}$  are calculated according to 1-D stratified structure [26]. The refractive indices of subwavelength structure for TE and TM polarizations can be calculated from the following equations:

$$\begin{aligned} \text{TE} : & \frac{\sqrt{n_{\text{si}}^2 - n_{\text{TE}}^2}}{n_{\text{si}}^2} \tan \left( \frac{\pi \sqrt{n_{\text{si}}^2 - n_{\text{TE}}^2} (\Lambda_{\text{sub}} - W_{\text{sub}})}{\lambda} \right) \\ & = - \frac{\sqrt{n_{\text{hole}}^2 - n_{\text{TE}}^2}}{n_{\text{hole}}^2} \tan \left( \frac{\pi \sqrt{n_{\text{hole}}^2 - n_{\text{TE}}^2} W_{\text{sub}}}{\lambda} \right) \end{aligned} \quad (1)$$

$$\begin{aligned} \text{TM} : & \sqrt{n_{\text{si}}^2 - n_{\text{TM}}^2} \tan \left( \frac{\pi \sqrt{n_{\text{si}}^2 - n_{\text{TM}}^2} (\Lambda_{\text{sub}} - W_{\text{sub}})}{\lambda} \right) \\ & = - \sqrt{n_{\text{hole}}^2 - n_{\text{TM}}^2} \tan \left( \frac{\pi \sqrt{n_{\text{hole}}^2 - n_{\text{TM}}^2} W_{\text{sub}}}{\lambda} \right) \end{aligned} \quad (2)$$

where  $n_{\text{TE}}$  and  $n_{\text{TM}}$  denote refractive indices of the subwavelength structure for TE and TM polarizations, respectively, while  $n_{\text{si}}$  and  $n_{\text{hole}}$  are the refractive indices of silicon and material inside the hole respectively. Since a 2-D PC lattice of holes in a dielectric supports TE polarization, (1) is selected for design. And considering fabrication yield and repeatability limitations, we set the trench width  $W_{\text{sub}} = 100 \text{ nm}$  and thus we can fix the parameter  $\Lambda_{\text{sub}} = 294 \text{ nm}$  which corresponds to a filling factor around 34%.

### B. Design Principles of Photonic Crystal Microcavities for Sensing

The device investigated consists of a  $Ln$  type PC microcavity side coupled to a  $W1$  type photonic crystal waveguide (PCW), where  $n$  denotes the number of missing air holes along the  $\Gamma-K$  lattice direction in a triangular lattice photonic crystal and  $W1$  denotes that the width of the PCW is  $\sqrt{3} a$  where  $a$  is the lattice constant. The schematic of the PC microcavity coupled waveguide device is shown in Fig. 2(a).

The total quality factor  $Q_T$  of the resonance mode of a PC microcavity side coupled to a PCW, which is related to the photon lifetime  $\tau_p$ , at frequency  $\omega$  by  $Q_T = \omega \tau_p$  is given by

$$\frac{1}{Q_T} = \frac{1}{Q_i} + \frac{1}{Q_R} + \frac{1}{Q_{\text{WG}}} \quad (3)$$

where  $Q_R = \omega \tau_R$ ,  $Q_i = \omega \tau_i$ , and  $Q_{\text{WG}} = \omega \tau_{\text{WG}}$ ,  $\tau_R$ ,  $\tau_i$  and  $\tau_{\text{WG}}$  represent time constants for the radiation loss, intrinsic cavity loss and waveguide loss respectively.  $\tau_R$  is given by:

$$\frac{1}{\tau_R} = \frac{P_R}{W_E} \quad (4)$$

where  $P_R$  denotes the total power radiated by the cavity and  $W_E$  denotes the stored energy in the cavity which is proportional to the cavity mode volume. We have shown previously [23] that increasing the length of the PC microcavity increases  $W_E$ . An

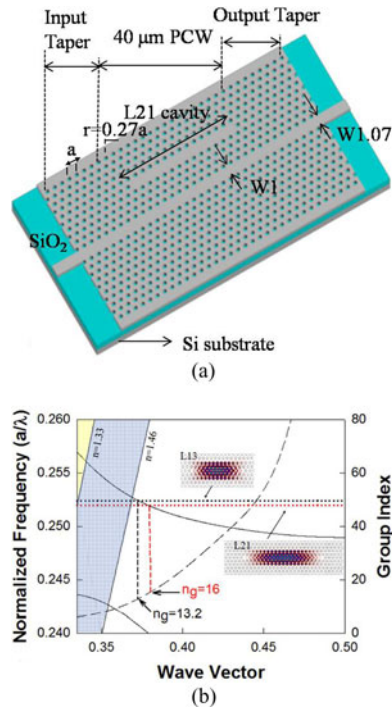


Fig. 2. (a) A schematic of photonic crystal microcavity device, (b) dispersion diagram of W1 PCW in water. The W1 guided mode is shown together with frequencies of resonant modes for L13 and L21 PC microcavities by black and red dashed lines respectively. The mode profiles are shown in insets.

increased cavity length also lowers the normalized frequency of the resonant mode in the photonic band gap leading to a decrease in the fraction of the optical mode above the bottom oxide cladding light line, and a corresponding decrease in  $P_R$ . Both factors lead to an increase in the effective Q. At the same time, increasing the length of the PC microcavity increases the analyte overlap with the resonance mode of the PC microcavity. Since the sensitivity of the device is determined by the resonance wavelength shift needed to observe the smallest change in concentration, a large resonance wavelength shift is desired for a given concentration of chemicals or biomolecules. The microcavity resonance Q and the analyte overlap with the resonance mode both determine the resonance wavelength shift and hence the sensitivity of the device.

We previously showed that in biosensing microarrays, where multiple sensor spots must be coated with unique immobilized antibodies, the method of dispensing the antibodies to be immobilized such as via ink-jet printing or by using microfluidic channels, determines the density of integration. The diameter of the dispensed spot in ink-jet printing is  $35\ \mu\text{m}$  in our system with a  $50\ \mu\text{m}$  center-to-center spacing between individual dispensed spots [23]. The diameter of  $35\ \mu\text{m}$  thus determines the upper limit of miniaturization in biosensing microarrays. We take advantage of the biopatterning engineering limitation to derive the dual benefits of a longer cavity design resulting in higher Q and a larger optical mode overlap with the analyte, to achieve higher sensitivities.

The simulated dispersion diagram of a W1 PCW is shown in Fig. 2(b). The resonance frequencies of the L13 and L21 PC microcavities are shown by the dotted black and dotted red lines

respectively. As the cavity size increases from L13 to L21, the resonance frequency moves closer to the band edge and  $P_R$  decreases. Since  $W_E$  is larger for the L21 PC microcavity,  $Q_R$  is effectively increased. As observed from Fig. 2(b), the group index of the W1 PCW at the coupling frequencies is higher for the L21 ( $n_g = 16$ ) compared to the L13 ( $n_g = 13.2$ ) PC microcavity. Enhanced optical coupling from the waveguide to the microcavity leads to enhanced light-matter interaction thus improving sensitivity as we have shown elsewhere [27].

In an uncoupled cavity, increasing the length of the PC microcavity increases the total Q of resonance modes. However, simply increasing the length of the microcavity from L13 to L21 based on (4) does not increase  $Q_T$  for the resonance modes of interest in the cavity-waveguide architecture. A longer cavity leads to increased leakage from the cavity to the PCW leading to lower  $Q_{WG}$  which lowers the effective  $Q_T$ . A high  $Q_T$  is desirable since it enables smaller changes in concentration to be detected. Hence, an optimum design requires optimizing the cavity-waveguide coupling for high Q and high sensitivity, in addition to other factors such as the magnitude of slow light in the coupling waveguide that we have discussed elsewhere [27]. To optimize  $Q_T$  while enhancing sensitivity, the PC microcavity is moved laterally away from the PCW to increase  $Q_{WG}$ . In this paper, we further investigated the effect of the lateral spacing between the cavity and the waveguide on  $Q_T$  and sensitivity of the L21 PC microcavity and engineered an optimized spacing to achieve the highest  $Q_T$ .

### III. DEVICE FABRICATION AND CHARACTERIZATION

#### A. Fabrication

The devices were fabricated on silicon on insulator (SOI) wafer with 250 nm top silicon layer and  $3\ \mu\text{m}$  buried oxide. PC waveguides, PC impedance tapers to minimize reflection loss, strip waveguides and SWG couplers are patterned simultaneously in one step with e-beam lithography using ZEP-520 A e-beam resist followed by reactive ion etching using  $\text{Cl}_2/\text{HBr}$ . The diameter of PC holes is 216 nm with 393 nm period while subwavelength structure has air holes with 100 nm by 367.5 nm in dimension. The whole chip shown in Fig. 3(a) is then coated with  $5\ \mu\text{m}$  thick SU8 in order to protect the SWG coupler from any interference during biosensing and an open channel is next patterned on top of the PCW region for sensing purpose. SEM images of the fabricated L21 type PC microcavity and SWG coupler are shown in Fig. 3. For measurement ease, the total length of the device between the input and output SWG couplers is 1 cm.

#### B. Characterization

The measurement setup has been described in a previous paper [15]. Input TE polarized light is coupled to the input SWG with a polarization maintaining single mode fiber. Light is coupled out of the output SWG via a standard single mode fiber. Light is guided in and out of the PCW by ridge waveguide with PC group index taper to enable high coupling efficiency into the slow light guided mode. The group index taper can be done by tuning the hole sizes [28] or the width of the PCW.

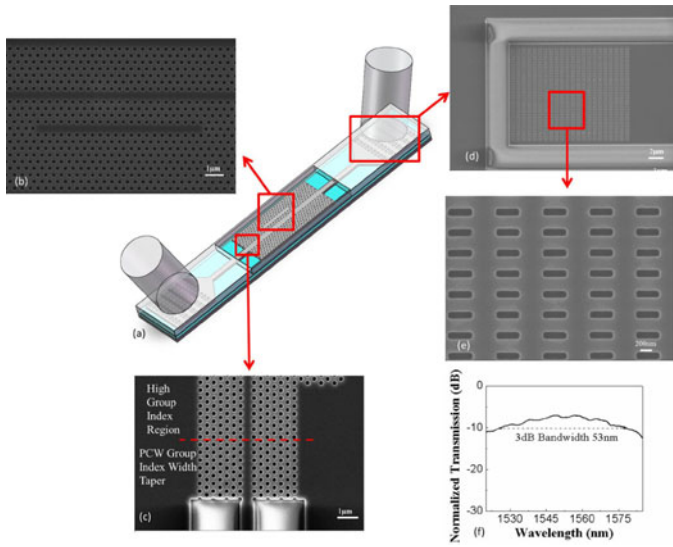


Fig. 3. (a) Schematic of the whole device, (b) close up of the L21 PC microcavity which is located four rows away from a W1 PCW, (c) SEM picture of the fabricated PCW device showing the PCW adiabatic group index taper achieved by gradually increasing the widths of the first eight periods of PCW to reduce the group index. The bottom cladding of silicon dioxide ( $n = 1.46$ ) is kept intact to enable robust devices with high yield. The SWG coupler is firstly characterized by measuring the insertion loss of fiber-to-device-to-fiber. The coupling efficiencies of two couplers are assumed as equal. In Fig. 3(f), the grating efficiency curve indicates that the peak efficiency for one SWG coupler is around  $-7$  dB which corresponding to 20% efficiency at 1550 nm. The 3 dB bandwidth is around 53 nm. The efficiency is lower than air-clad SWGs reported previously [15] due to the SU8 top cladding of grating region in devices for chemical and biological sensing. The SU8 serves as the protection layer to eliminate any interference to the grating signal and resultant coupling efficiency due to analyte spreading during biosensing. The output spectrum of the grating was used as reference to normalize transmission data from microcavity coupled W1 PCW devices on the same chip.

Position shifting is a more fabrication friendly approach [29], since the accurate control of several different hole sizes requires more optimizations of dose matrices in lithography. The PCW adiabatic group index taper, shown in Fig. 3(c), is achieved by gradually increasing the widths of the first eight periods of PCW to reduce the group index. The bottom cladding of silicon dioxide ( $n = 1.46$ ) is kept intact to enable robust devices with high yield. The SWG coupler is firstly characterized by measuring the insertion loss of fiber-to-device-to-fiber. The coupling efficiencies of two couplers are assumed as equal. In Fig. 3(f), the grating efficiency curve indicates that the peak efficiency for one SWG coupler is around  $-7$  dB which corresponding to 20% efficiency at 1550 nm. The 3 dB bandwidth is around 53 nm. The efficiency is lower than air-clad SWGs reported previously [15] due to the SU8 top cladding of grating region in devices for chemical and biological sensing. The SU8 serves as the protection layer to eliminate any interference to the grating signal and resultant coupling efficiency due to analyte spreading during biosensing. The output spectrum of the grating was used as reference to normalize transmission data from microcavity coupled W1 PCW devices on the same chip.

20 L13 PC microcavity coupled to W1 PCW devices were fabricated on two chips and measured in water. 19 out of 20 devices show good waveguide transmission spectra with clear and sharp transmission band edges in which the power drops more than 20 dB within a 5 nm wavelength range over the transition from wavelength transmission band to transmission band gap. The spectra from each of the nineteen devices in water are shown in Fig. 4. No output power was observed from the 20th device due to the stitching effect in the input grating coupler that can be seen in the extreme right bottom segment of Fig. 4 as a dark green line at the center of the grating.

Ten L21 devices are fabricated on a chip and characterized under water and glycerol. Nine out of ten devices provide

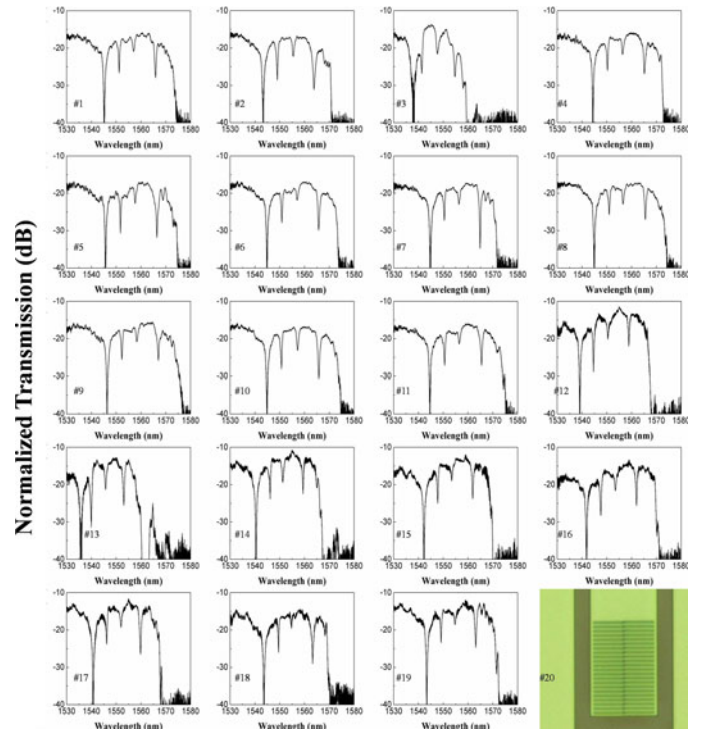


Fig. 4. Experimental transmission spectra in water of 19 devices comprising W1 PCW coupled to L13 PC microcavities. Extreme right bottom inset shows microscope image of stitching observed on 20th device.

similar output power at 1550 nm as well as good waveguide transmission spectrum characteristics with sharp resonance peaks as observed in Fig. 5(a). The transmission from the 10th device shows lower output power as in Fig. 5(b) and several Fabry–Perot type resonance modes are seen in the transmission spectrum in Fig. 5(c) superimposed with the L21 PC microcavity resonance modes. We believe that the transmission characteristics of Device 5 are contributed by a defect on the strip waveguide section, as shown in the SEM image in Fig. 5(d). For all working devices, the absolute wavelength positions of all the resonant modes and band edges are nearly same and the slight difference may be due to fabrication fluctuations or the different thicknesses of the SOI wafer at the specific location of the photonic crystal pattern on the SOI wafer.

A close examination of the L21 PC microcavity spectra in Fig. 5(a) indicates that the resonance closest to the transmission band edge is missing from Devices 2 and 8. The missing mode is labeled A in the L21 spectrum shown in Device 1 in Fig. 5(a). For each of devices 2 and 8, it is also observed that the quality factor of mode C is also reduced. However, quality factors of modes B and D in devices 2 and 8 are similar to the Q in other devices in Fig. 5(a) where mode A is observed. The electric field intensity profiles of modes A, B, C and D for the L21 PC microcavity are calculated using RSoft 2D BandSolve and shown in Fig. 5(e). While no visual confirmation could be achieved from a top view SEM image of the L21 PC microcavities in devices 2 and 8, an examination of the mode field profile suggests that fabrication induced variations could exist in the region of the air holes in the immediate vicinity of the photonic crystal microcavity within the red dashed square demarcated in Mode B in Fig. 5(e), the

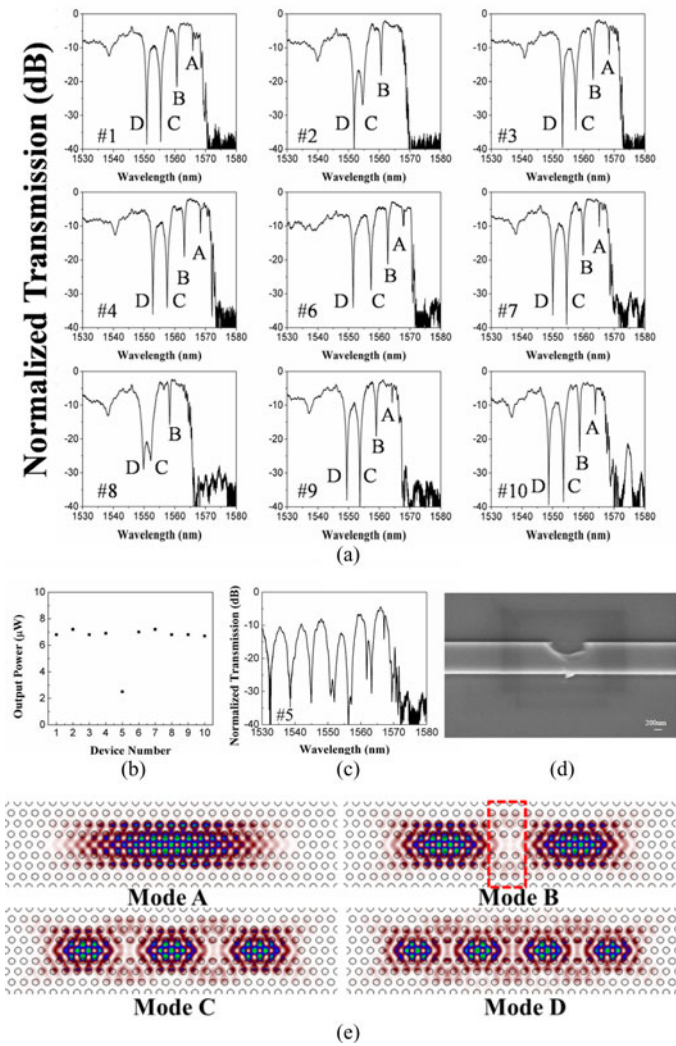


Fig. 5. (a) Experimental transmission spectra in glycerol of nine out of ten devices comprising W1 PCW coupled to L21 PC microcavities. (b) Output power of all ten L21 devices, (c) transmission spectrum of L21 device #5 (d) SEM image of defect on ridge waveguide section at the input of PCW in device 5. (e) Electric field intensity profiles of the resonant modes A, B, C and D in (a).

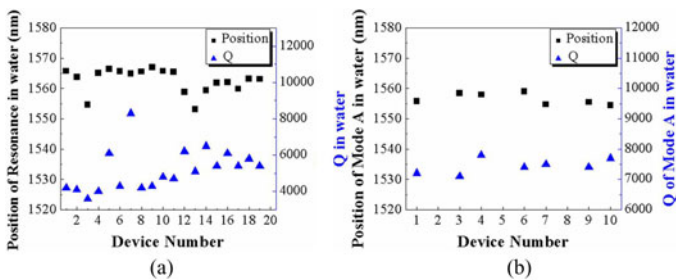


Fig. 6. Distribution of  $Q$  and absolute wavelength position in water of resonance modes closest to the band edge for (a) L13 and (b) L21 PC microcavities in Fig. 4 and Fig. 5.

dashed region being the only region common to both modes A and C, where modes B and D have low electric field intensities.

Fig. 6(a) and (b) shows the distribution of  $Q$  in water for all L13 and L21 devices investigated in Figs. 4 and 5 respectively. For L21 devices, excluding devices #2, #5 and #8, a narrow distribution of  $Q$  ( $7,300 \pm 500$ ) and a narrow distribution of

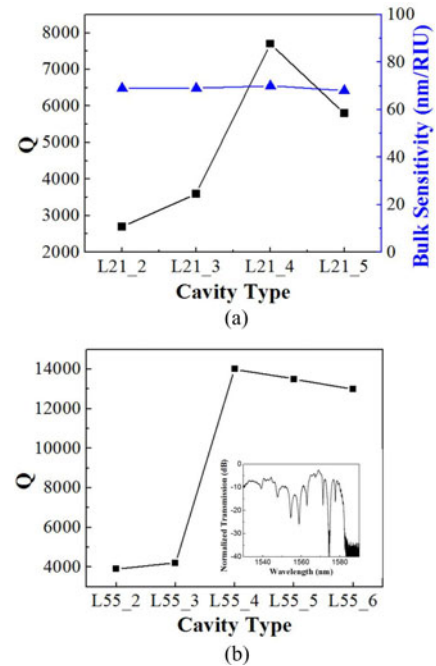


Fig. 7.  $Q$ -factors (black squares) and bulk sensitivity (blue triangles) variation of (a) L21 microcavity side coupled to W1 PCW in water versus microcavity location change (L21\_2 represents L21 microcavity 2 rows away from the PCW) and (b) L55 microcavity side coupled to W1 PCW in water versus microcavity location change. The inset is the transmission spectrum of L55 with cavity located four rows away from the PCW.

absolute wavelength of the resonance mode A ( $\pm 2$  nm) is observed. For L13 devices, we exclude devices #3, #7 and #13, in addition to #20, since extremums are observed in one or both of  $Q$  and absolute wavelength position. For the remaining devices, the distribution of  $Q$  is ( $5,300 \pm 1200$ ) while the variation in absolute wavelength position is  $\pm 4$  nm. We note here that the  $Q \sim 5300 \pm 1200$  observed in water in L13 PC microcavities in the present devices with 250 nm silicon device layer is lower than  $Q \sim 13,000$  previously demonstrated with SOI devices with 230 nm device silicon capped by 20 nm  $\text{SiO}_2$ . [23] With respect to the absolute wavelength, it is to be noted that a distribution of  $\pm 5$  nm is allowable for these sensor structures since the intrinsic material absorption of silicon and the ambient PBS can be assumed to be nearly constant over this narrow wavelength range so as not to affect the  $Q$  appreciably. Also, the device operating principle requires the measurement of relative wavelength shift and hence the absolute wavelength variation within  $\pm 5$  nm can be tolerated. From considerations of purity of device transmission spectrum, resonance mode quality factor and absolute resonance wavelength position, the yields for L13 and L21 devices are thus 80% and 70% respectively.

As discussed in Section II, the loss from the PC microcavity into the PCW plays a critical role in the total loss of the PC microcavity, and contributes a term  $Q_{WG}$  to (3). Since  $Q_{WG}$  is primarily determined by the number of periods between the PC microcavity and the PCW, we fabricated devices in which the L21 PC microcavity is located 2, 3, 4 and 5 rows away from the PCW. Fig. 7(a) shows the experimental  $Q$  ( $=\lambda/\Delta\lambda$ ).

As the L21 PC microcavity moves away from the PCW,  $Q$  increases indicating reduced cavity to waveguide loss and

improved optical confinement by the photonic crystal microcavity. At the same time, the normalized frequency of the resonance mode increases as the dielectric fraction in the vicinity of the PC microcavity decreases as it moves away from the PCW. From the dispersion diagram in Fig. 2(b), a higher normalized frequency implies more radiation loss as a greater fraction of the optical mode is above the light line, which will decrease  $Q_R$ .  $Q_i$  will also decrease as the PC microcavity moves further away from the W1 PCW due to the increased mode overlap with surface roughness of more surrounding holes.

A limiting situation is reached when the PC microcavity is located more than four rows away from the PCW. The increase of  $Q_R$  and  $Q_i$  dominate over the increase in  $Q_{WG}$  and hence the effective  $Q_T$  decreases. Since the loss rate from the cavity to the waveguide and vice-versa is directly proportional to the cavity length, the highest Qs will be achieved at different distance of the cavities from the PCW for cavities of different lengths such as L13 and L21. The L13 PC microcavities in Fig. 4 were considered 2 rows away laterally from the W1 PCW. For our L21 PC microcavity, it is observed that when the PC microcavity is located 4 rows away from the PCW, Q reaches a maximum. The Q of a L21 PC microcavity located 2 rows away from the W1 PCW ( $Q \sim 2,500$ ) is lower than the Q of a L13 PC microcavity located 2 rows away from the W1 PCW. Hence, a simple increase of the cavity length does not increase Q; other factors such as the cavity-waveguide coupling determined by  $Q_{WG}$  need to be engineered. The bulk sensitivities of the L21 PC microcavity devices shown in Fig. 7(a), change negligibly as the L21 PC microcavity is moved away from the W1 PCW, since the mode volume of the microcavity changes negligibly as the cavity is moved farther away from the W1 PCW. However, a larger Q enables smaller changes in analyte concentration to be accurately measured.

A similar effect is observed with a L55 type PC microcavity with 55 missing holes along the length of a W1 PCW. L55 PC microcavity devices were fabricated with the microcavity located 2, 3, 4, 5, and 6 rows away from the PCW on one chip. As shown in Fig. 7(b), the Q of the resonance closest to the transmission band edge varies and reaches a maximum ( $\sim 14,000$ ) when the PC microcavity is located 4 rows away from the W1 PCW. The inset shows the transmission spectrum of W1 PCW with L55 PC microcavity 4 rows away from the PCW.

### C. Biosensing

To enable the biosensing experiments, the devices were first functionalized to enable receptor antibody/protein immobilization on the silicon substrate. The biomolecule functionalization process has been described in detail in ref. [22]. 60  $\mu\text{l}$  target protein Avidin (67kDa) solution was directly dispensed from a micro-pipette. The diameter of the dispensed spot on silicon is around 8 mm. During biosensing measurements, after each new addition of a new concentration of target protein, the device is washed three times in PBS before the effective resonance wavelength shift is measured in PBS. Experimental resonance transmission spectra observed when avidin binds to the probe biotin is shown in Fig. 8(a). The lowest concentrations are shown

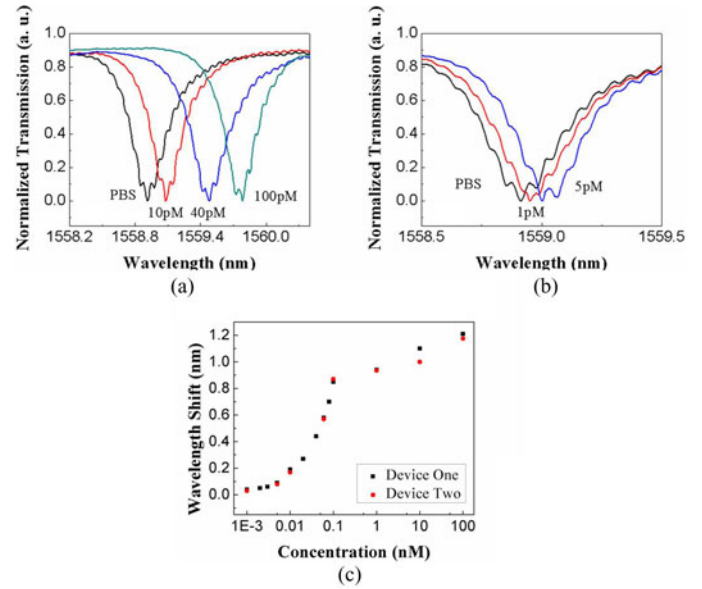


Fig. 8. Experimental drop resonance spectra for the binding between avidin to biotin ( $K_d \sim 10^{-15}$  M) (a) between 0 pM to 100 pM and (b) at the lower concentration range between 0 pM and 5 pM. (c) Experimental spectral shift for various concentrations of avidin binding to biotin in two L21 (red circles and black squares) PC microcavities.

separately in Fig. 8(b) for clarity. In both Fig. 8(a) and (b), ripples observed are due to Fabry–Perot effects which become larger as the resonance modes come closer to the transmission band edge due to the larger group index mismatch between the PCW and the ridge waveguides as shown in Fig. 2(b). Work is currently in progress to reduce the ripples in the resonance via advanced group index taper engineering.

At the lowest concentration of 1 pM for L21 PC microcavity, which corresponds to 67 pg/ml avidin, a resonance wavelength shift of 0.04 nm was observed as shown in Fig. 8(b). In the L21 PC microcavity, (integrating over an area where the E-field intensity is more than 50% of the maximum value and including the entire internal surface area of the holes along the periphery of the photonic crystal microcavity in the  $\Gamma$ –K orientation where the E-field intensity is more than 50% over a fraction of the periphery of the hole) [30], from Fig. 2(b), the optical mode overlaps a surface area on the chip of  $13.62 \mu\text{m}^2$ . The actual real estate coverage of the optical mode on the chip is approximately  $5.7 \mu\text{m}^2$  slightly larger than the L13 PC microcavity [22]. By assuming uniform surface coverage, the detection limit for surface density is  $80 \text{ fg}/\text{mm}^2$ . Fig. 8(c) plots the resonant wavelength shift  $\Delta\lambda$  as a function of concentration. As observed in Fig. 8(c), at the concentrations bigger than 100 pM, binding sites of biotin are increasingly occupied by avidin and the resonance wavelength shift gradually saturated. To verify sensing repeatability, two identical L21 PC microcavity coupled PCW devices were fabricated and tested. Both show similar wavelength shift when different concentrations were added. These results further prove the measurement repeatability of L21 PC microcavity devices. A control experiment is done to verify that no resonance wavelength shift occurs in a control PC microcavity coated with BSA when different concentrations of avidin are introduced.

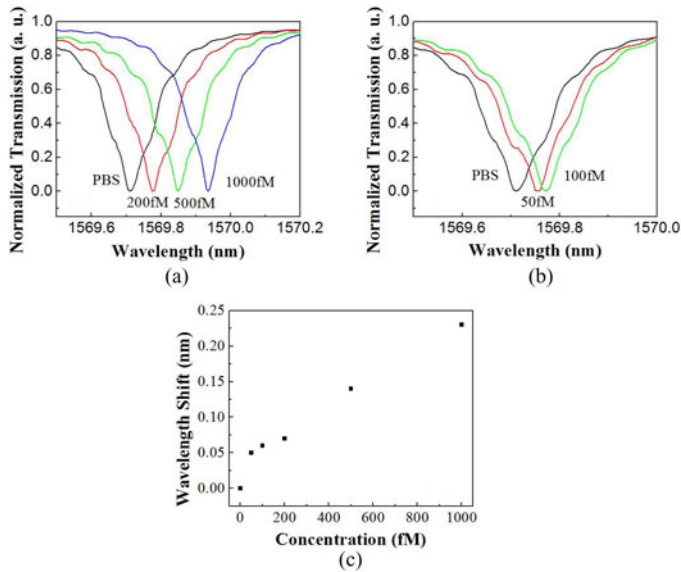


Fig. 9. Experimental drop resonance spectra for the binding between avidin to biotin ( $K_d \sim 10^{-15}$  M) on L55 PC microcavity device (a) between 0 fM to 1000 fM and (b) at the lower concentration range between 0 fM and 100 fM. (c) Experimental spectral shift for various concentrations of avidin binding to biotin in L55 PC microcavities.

The L55 PC microcavity has a larger mode volume and thus a larger sensing area. The L55 cavity length is approximately  $23 \mu\text{m}$ , which is less than the  $35 \mu\text{m}$  drop size of the inkjet-printed probe protein. The biosensing on this device followed the same procedure as for L13 and L21 devices. The resonance wavelength spectral shift curves with different concentrations are shown in Fig. 9(a) and (b) for the L55 PC microcavity. Fig. 9(c) shows the change in resonance wavelength as a function of concentration. We successfully detected avidin-biotin binding at the concentration of 50 femto-Molar ( $3.3 \text{ pg/ml}$ ) with the L55 PC microcavity, more than an order of magnitude better than L21.

The wavelength shifts observed in the control experiments are within  $0.02 \text{ nm}$ , which is within the wavelength accuracy limit of our optical spectrum analyzer. Since  $dn/dT = 1.87 \times 10^{-4}$  at  $295 \text{ K}$  for silicon, the biomolecule sensing measurement limit of the shift  $\Delta\lambda$  is  $0.01 \text{ nm}$  [23] which is lower than the accuracy limit of our optical spectrum analyzer. Hence there is no need for temperature compensation. Thus, in all experiments, resonance wavelength shifts greater than  $0.02 \text{ nm}$  were considered as the signature of a binding event between the receptor capture biomolecule (biotin) and its specific conjugate (avidin).

## IV. DISCUSSION

### A. Yield and Quality Comparison Between End-Fire Coupling and Grating Coupling

As seen from Figs. 4 and 5(a), fabrication yield rate is greatly improved using SWG couplers in our devices. High quality spectral can be observed from all the working devices with clean curve, sharp resonances and high extinction ratio between pass band and band gap.

The SWG serves as a wave front scrambler and therefore an antireflection layer. The SWG destroys the wave front of incident light, reduces the reflection from SOI chip and the oblique incident angle also lowers the Fabry-Perot effects thereby greatly eliminating the fringes and enhancing the coupling efficiency into SOI chip. Secondly, the extinction ratio between pass band and band gap reduces quite a lot for end-fire coupling method compared with subwavelength grating coupler. While an external polarization filter is employed in end-fire coupling, the polarization contrast between TE and TM of external filters determined the final polarization extinction ratio. In contrast, the SWG designed specifically for TE polarization appears to be an additional effective polarization filter and blocks the remaining TM polarized light from the incident fiber. Thus the final polarization extinction ratio is the product of polarization extinction ratios of the external filter and the SWG. Coupling light into PCWs through SWG couplers thus dramatically improves spectral quality and measurement yield of working devices, as noted in Fig. 6. Since the SWG couplers can be fabricated simultaneously with PCWs, there are no extra steps needed. No cleaving of waveguides is necessary as in end-fire coupling, which usually would require further post-processing such as polishing of facets for better yield. SWGs therefore significantly improve the yield of devices with good spectral characteristics useful for biosensing experiments, which is the better measure of working device yield compared to just fabrication yield.

It may be argued that 30 devices are insufficient to reach a conclusion on yield. Yield information on photonic crystal devices is generally not reported in the literature; our own experience together with discussions with our research peers indicate that in general, yield of photonic crystal device is quite poor. Our yields of 80% by integrating SWG couplers with PC devices therefore represent significant milestone not only in PC biosensors but in PC based nanophotonics, in general. We believe the results can be easily validated in a commercial foundry with large sample size.

### B. Comparison Between L13 and L21 PC Microcavity

The comparison of bulk sensitivity of L13 and L21 PC microcavities coupled to W1 PCW is shown in Fig. 10(a) and (b) respectively. Comparing the wavelength shifts of the resonance mode in water and glycerol, the shift for L13 is  $8.6 \text{ nm}$  ( $66 \text{ nm/RIU}$ ), while the L21 shift is  $9.6 \text{ nm}$  ( $74 \text{ nm/RIU}$ ). The resonance modes of interest in these structures are the modes located closest to the band edge [mode A for L21 PC microcavity as in Fig. 6(a)].

For the L13 PC microcavity, as observed previously [22] the offset of the resonance mode from the band edge is around  $6 \text{ nm}$  while for L21 the offset is approximately  $4 \text{ nm}$ . Considering the same absolute normalized frequency of the transmission band edge in Fig. 2(b), a resonance mode located closer to the W1 PCW transmission band edge has lower fraction of radiation loss  $P_R$ . A longer L21 PC microcavity has more stored energy  $W_E$  per unit volume than the L13 PC microcavity. A lower  $P_R$  and higher  $W_E$  both contribute to higher  $Q_R$  for the L21 PC microcavity compared to the L13 PC microcavity. The L21 PC

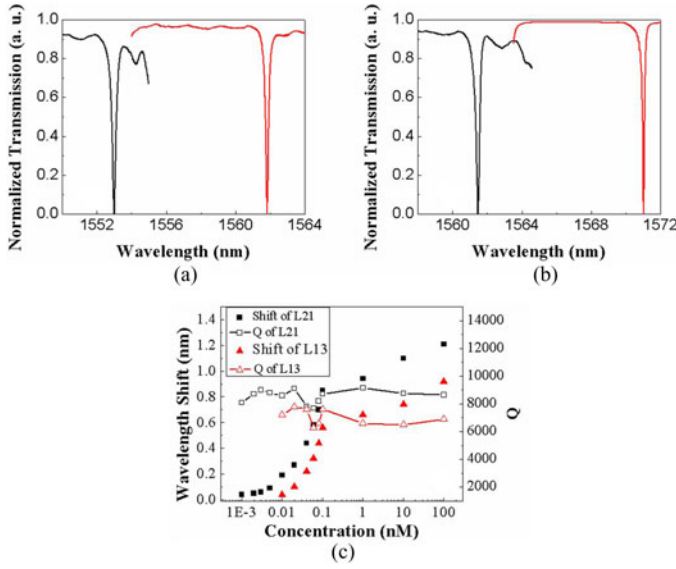


Fig. 10. (a) Experimental spectra of (a) L13 and (b) L21 PC microcavities showing shift of resonance mode closest to the band edge in water (black) versus glycerol (red), (c) Experimental spectral shift for various concentrations of avidin binding to biotin in L13 (filled triangles) and L21 (filled squares) PC microcavities. Experimental Q variation for L13 (open triangles) and L21 (open squares) devices are also shown.

microcavity also has a larger optical mode volume than L13 which enables greater optical mode overlap with any analyte than in L13. It can be reasonably expected that  $Q_i$  will be higher in L13 than in L21 due to the smaller optical mode volume which reduces the surface roughness scattering loss.

Finally, we consider that  $Q_{WG}$  is inversely proportional to the length of the optical microcavity and directly proportional to the group velocity in the coupled W1 PCW. Both factors indicate a lower  $Q_{WG}$  in L21 compared to L13 PC microcavities. The lowering effect of  $Q_{WG}$  was compensated by moving the L21 PC microcavity four rows away from the W1 PCW. Microcavity engineering thus resulted in resonances in L21 PC microcavities with  $Q \sim 7,300 \pm 500$  in water higher than  $Q \sim 5,300 \pm 1,200$  in L13 PC microcavities in addition to larger optical mode overlap with the analyte. As observed in Fig. 10(c), the Q of L21 PC microcavities is generally higher than that of L13 PC microcavities when measured as a function of increasing concentration of dispensed antibodies. The variation of Q in each case is within the range typically observed for both L13 and L21 PC microcavities. In addition, as shown in Fig. 2(b), the magnitude of slowdown factor in the coupled W1 PCW at the resonance mode frequency of interest is higher in L21 than in L13 PC microcavities, which also contributes to higher sensitivity [27]. The combined effects of higher Q, higher optical mode overlap and larger slow light effect in the coupled waveguide at the resonance frequency of interest, in L21 PC microcavities compared to L13 PC microcavities, leads to higher biosensing sensitivity in L21 compared to L13 as shown in the plot in Fig. 10(c) for different concentrations of avidin binding to receptor capture biotin.

A similar analysis was performed for L55 PC microcavities. The resonance mode of interest in the L55 PC microcavity is

TABLE I  
COMPARISON OF DIFFERENT TYPES OF PC MICROCAVITIES

Microcavity Type	Detection Limit (Molar)	Q	Location of cavity (rows offset from PCW)	Yield
L13	$10^{-11}$	5300 $\pm$ 1200	2	80%
L21	$10^{-12}$	7300 $\pm$ 500	4	70%
L55	$5 \times 10^{-14}$	14000 $\pm$ 600	4	N/A

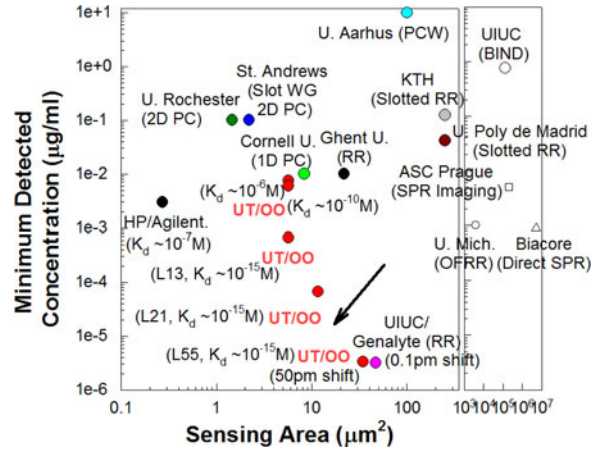


Fig. 11. Comparison of minimum experimentally demonstrated detection limits versus other label-free optical platforms as a function of sensing area on chip. Red dots represent data obtained in our PC microcavity biosensors coupled to a W1 PCW.

offset  $\sim 3$  nm from the transmission band edge compared to a 4 nm offset of resonance A of the L21 PC microcavity. As a result, the group index of light in the propagating waveguide is even larger than in L21. Coupled with higher Q and higher optical mode overlap than L21, the L55 PC microcavity consequently experimentally demonstrated a lower detection limit. Table I summarizes the characteristic of three types PC microcavities discussed in our paper.

It can be anticipated that linear PC microcavities longer than L55 will have better sensitivity than 50 femto-molar demonstrated here experimentally. From the perspective of limitations due to ink-jet printed spot size with  $35 \mu\text{m}$  diameter, for maximum usage of a particular type of probe antibody that interacts with the trapped optical mode in the vicinity of the sensing microcavity in a multiplexed assay, the length can be increased to beyond  $23 \mu\text{m}$  of our L55 PC microcavity.

In Fig. 11, we update the current status [22] of the minimum experimentally detected concentration of target biomolecules captured by a probe receptor, demonstrated in our PC microcavities side coupled to a W1 PCW, versus other label-free methods, including surface plasmon resonance devices [20], opto-fluidic ring resonators [31], ring resonator [18], [32], [33] and other photonic crystal (PC) devices [34]–[38], as function of sensing area. Compared to a 0.1 pm shift observed with a 60 fM concentration of streptavidin binding to biotin in a ring resonator with diameter  $30 \mu\text{m}$  [17], the  $23 \mu\text{m}$  long L55 PC microcavity

device demonstrated a 500 times larger resonance wavelength shift of 50 pm for the binding of avidin to biotin. A recent demonstration of sub-attomolar detection with PC nanolasers in an InP platform is not considered due to its incompatibility with biological buffers with salt ions [39]. The sensing area of our device is smaller than other techniques such as nano-hole plasmonic arrays [40], or surface enhanced Raman scattering sensors [41] at equivalent detected concentrations, which essentially interrogate the signal over a large number of hot spots to achieve published sensitivities

## V. CONCLUSION

In summary, we demonstrated an on-chip sensing system for high yield and high sensitivity biosensing combining sub-wavelength grating couplers and long linear PC microcavities side-coupled to a W1 PCW. In addition to high working device yields, of 80% for L13 devices and 70% for L21 devices, subwavelength grating couplers also significantly improve the quality of the resonance spectrum. The quality factor of L21 and L55 PC microcavities coupled to the W1 PCW was increased by engineering the cavity-waveguide coupling along with the length of the microcavity. We experimentally detected the binding of 1 pM and 50 femto-molar concentration of avidin to its specific conjugate biotin in PBS for L21 and L55 devices respectively, more than one order of magnitude higher than our previous demonstration [22] and with higher sensitivity and larger miniaturization than other competing technologies. Device miniaturization is still retained from the context of practical engineering limitations of biomolecule patterning in a biosensing microarray.

## REFERENCES

- [1] T. Shoji, T. Tsuchizawa, T. Watanabe, K. Yamada, and H. Morita, "Low loss mode size converter from 0.3  $\mu\text{m}$  square Si wire waveguides to single mode fibers," *Electron. Lett.*, vol. 38, pp. 1669–1670, 2002.
- [2] V. R. Almeida, R. R. Panepucci, and M. Lipson, "Nanotaper for compact mode conversion," *Opt. Lett.*, vol. 28, pp. 1302–1304, 2003.
- [3] K. K. Lee, D. R. Lim, D. Pang, C. Hoepfner, W.-Y. Oh, K. Wada, L. C. Kimerling, K. P. Yap, and M. T. Doan, "Mode transformer for miniaturized optical circuits," *Opt. Lett.*, vol. 30, pp. 498–500, 2005.
- [4] S. J. McNab, N. Moll, and Y. A. Vlasov, "Ultra-low loss photonic integrated circuit with membrane-type photonic crystal waveguides," *Opt. Exp.*, vol. 11, pp. 2927–2939, 2003.
- [5] D. Taillaert, F. Van Laere, M. Ayre, W. Bogaerts, D. Van Thourhout, P. Bienstman, and R. Baets, "Grating couplers for coupling between optical fibers and nanophotonic waveguides," *Jpn. J. Appl. Phys.*, vol. 45, pp. 6071–6077, 2006.
- [6] Y. Tang, Z. Wang, L. Wosinski, U. Westergren, and S. He, "Highly efficient nonuniform grating coupler for silicon-on-insulator nanophotonic circuits," *Opt. Lett.*, vol. 35, pp. 1290–1292, 2010.
- [7] G. Roelkens, D. Vermeulen, D. Van Thourhout, R. Baets, S. Brision, P. Lyan, P. Gautier, and J. M. Fedeli, "High efficiency diffractive grating couplers for interfacing a single mode optical fiber with a nanophotonic silicon-on-insulator waveguide circuit," *Appl. Phys. Lett.*, vol. 92, pp. 131101-1–131101-3, 2008.
- [8] F. Van Laere, G. Roelkens, M. Ayre, J. Schrauwen, D. Taillaert, D. Van Thourhout, T. F. Krauss, and R. Baets, "Compact and highly efficient grating couplers between optical fiber and nanophotonic waveguides," *J. Lightw. Technol.*, vol. 25, pp. 151–156, 2007.
- [9] M. Antelius, K. B. Gylfason, and H. Sohlström, "An apodized SOI waveguide-to-fiber surface grating coupler for single lithography silicon photonics," *Opt. Exp.*, vol. 19, pp. 3592–3598, 2011.
- [10] F. Li, L. Wu, T. Li, M. Dubinovsky, S. Tang, and R. T. Chen, "Unidirectional surface-normal waveguide grating coupler for wafer-scale MCM interconnect," *Proc. SPIE 3005*, pp. 136–142, 1997.
- [11] L. Liu, M. Pu, K. Yvind, and J. M. Hvam, "High-efficiency, large-bandwidth silicon-on-insulator grating coupler based on a fully-etched photonic crystal structure," *Appl. Phys. Lett.*, vol. 96, pp. 051126-1–051126-3, 2010.
- [12] R. Halir, P. Cheben, S. Janz, D.-X. Xu, Í. Molina-Fernández, and J. G. Wangüemert-Pérez, "Waveguide grating coupler with subwavelength microstructures," *Opt. Lett.*, vol. 34, pp. 1408–1410, 2009.
- [13] R. Halir, P. Cheben, J. H. Schmid, R. Ma, D. Bedard, S. Janz, D. X. Xu, A. Densmore, J. Lapointe, and Í. Molina-Fernández, "Continuously apodized fiber-to-chip surface grating coupler with refractive index engineered subwavelength structure," *Opt. Lett.*, vol. 35, pp. 3243–3245, 2010.
- [14] C. Xia and H. K. Tsang, "Nanoholes grating couplers for coupling between silicon-on-insulator waveguides and optical fibers," *IEEE Photon. J.*, vol. 1, no. 3, pp. 184–190, Sep. 2009.
- [15] X. Xu, H. Subbaraman, J. Covey, D. Kwong, A. Hosseini, and R. T. Chen, "Complementary metal–oxide–semiconductor compatible high efficiency subwavelength grating couplers for silicon integrated photonics," *Appl. Phys. Lett.*, vol. 101, pp. 031109-1–031109-3, 2012.
- [16] H. Subbaraman, X. Xu, J. Covey, and R. T. Chen, "Efficient light coupling into in-plane semiconductor nanomembrane photonic devices utilizing a sub-wavelength grating coupler," *Opt. Exp.*, vol. 20, pp. 20659–20665, 2012.
- [17] M. Iqbal, M. A. Gleeson, B. Spaugh, F. Tybor, W. G. Gunn, M. Hochberg, T. Baehr-Jones, R. C. Bailey, and L. C. Gunn, "Label-free biosensor arrays based on silicon ring resonators and high-speed optical scanning instrumentation," *IEEE J. Sel. Top. Quant. Electron.*, vol. 16, no. 3, pp. 654–661, May/June 2010.
- [18] C. F. Carlborg, K. B. Gylfason, A. Kazmierczak, F. Dortu, M. J. Banuls Polo, A. Maquieira Catala, G. M. Kresbach, H. Sohlstrom, T. Moh, L. Vivien, J. Popplewell, G. Ronan, C. A. Barrios, G. Stemme, and W. van der Winngaart, "A packaged optical slot-waveguide ring resonator sensor array for multiplex label-free assays in labs-on-chips," *Lab Chip*, vol. 10, pp. 281–290, 2010.
- [19] A. Densmore, M. Vachon, D. X. Xu, S. Janz, R. Ma, Y. H. Li, G. Lopinski, A. Delage, J. Lapointe, C. C. Luebbert, Q. Y. Liu, P. Cheben, and J. H. Schmid, "Silicon photonic wire biosensor array for multiplexed real-time and label-free molecular detection," *Opt. Lett.*, vol. 34, pp. 3598–3600, 2009.
- [20] H. Sipova, S. Zhang, A. M. Dudley, D. Galas, K. Wang, and J. Homola, "Surface plasmon resonance biosensor for rapid label-free detection of microribonucleic acid at subfemtomole level," *Anal. Chem.*, vol. 82, pp. 10110–10115, 2010.
- [21] B. S. Song, S. Noda, T. Asano, and Y. Akahane, "Ultra-high-Q photonic double heterostructure nanocavity," *Nat. Mater.*, vol. 4, pp. 207–210, 2005.
- [22] S. Chakravarty, Y. Zou, W. Lai, and R. T. Chen, "Slow light engineering for high Q high sensitivity photonic crystal microcavity biosensors in silicon," *Biosens. Bioelectron.*, vol. 38, pp. 170–176, 2012.
- [23] W. C. Lai, S. Chakravarty, Y. Zou, and R. T. Chen, "Silicon nanomembrane based photonic crystal microcavities for high sensitivity biosensing," *Opt. Lett.*, vol. 37, pp. 1208–1210, 2012.
- [24] Y. Zou, S. Chakravarty, W. Lai, C. Lin, and R. T. Chen, "Methods to array photonic crystal microcavities for high throughput high sensitivity biosensing on a silicon-chip based platform," *Lab Chip*, vol. 12, pp. 2309–2312, 2012.
- [25] P. Yeh, A. Yariv, and C.-S. Hong, "Electromagnetic propagation in periodic stratified media. I. General theory," *J. Opt. Soc. Amer.*, vol. 67, pp. 423–438, 1977.
- [26] S. M. Rytov, "Electromagnetic properties of a finely stratified medium," *Sov. Phys. J. Exp. Theor. Phys.*, vol. 2, pp. 466–475, 1956.
- [27] W.-C. Lai, S. Chakravarty, Y. Zou, and R. T. Chen, "Slow light enhanced sensitivity of resonance modes in photonic crystal biosensors," *Appl. Phys. Lett.*, vol. 102, pp. 041111-1–041111-4, 2013.
- [28] C. Y. Lin, X. Wang, S. Chakravarty, B. S. Lee, W. C. Lai, and R. T. Chen, "Wideband group velocity independent coupling into slow light silicon photonic crystal waveguide," *Appl. Phys. Lett.*, vol. 97, pp. 183302-1–183302-3, 2010.
- [29] S. A. Schulz, L. O'Faolain, D. M. Beggs, T. P. White, A. Melloni, and T. F. Krauss, "Dispersion engineered slow light in photonic crystals: A comparison," *J. Opt.*, vol. 12, pp. 104004-1–104004-10, 2010.
- [30] D. Dorfner, T. Zabel, T. Hürlimann, N. Hauke, L. Frandsen, U. Rant, G. Abstreiter, and J. Finley, "Photonic crystal nanostructures for optical

- biosensing applications,” *Biosens. Bioelectron.*, vol. 24, pp. 3688–3692, 2009.
- [31] H. Li and X. Fan, “Characterization of sensing capability of optofluidic ring resonator biosensors,” *Appl. Phys. Lett.*, vol. 97, pp. 011105-1–011105-3, 2010.
- [32] C. A. Barrios, “Optical slot-waveguide based biochemical sensors,” *Sensors*, vol. 9, pp. 4751–4765, 2009.
- [33] K. De Vos, I. Bartolozzi, E. Schacht, P. Bienstman, and R. Baets, “Silicon-insulator microring resonator for sensitive and label-free biosensing,” *Opt. Exp.*, vol. 15, pp. 7610–7615, 2007.
- [34] M. Lee and P. M. Fauchet, “Two-dimensional silicon photonic crystal based biosensing platform for protein detection,” *Opt. Exp.*, vol. 15, pp. 4530–4535, 2007.
- [35] C. Kang, C. T. Phare, Y. A. Vlasov, S. Assefa, and S. M. Weiss, “Photonic crystal slab sensor with enhanced surface area,” *Opt. Exp.*, vol. 18, pp. 27930–27937, 2010.
- [36] S. Mandal and D. Erickson, “Nanoscale optofluidic sensor arrays,” *Opt. Exp.*, vol. 16, pp. 1623–1631, 2008.
- [37] M. G. Scullion, A. Di Falco, and T. F. Krauss, “Slotted photonic crystal cavities with integrated microfluidics for biosensing applications,” *Biosens. Bioelectron.*, vol. 27, pp. 101–105, 2011.
- [38] S. Zlatanovic, L. W. Mirkarimi, M. M. Sigalas, M. A. Bynum, E. Chow, K. M. Robotti, G. W. Burr, S. Esener, and A. Grot, “Photonic crystal microcavity sensor for ultracompact monitoring of reaction kinetics and protein concentration,” *Sens. Actuators B*, vol. 141, pp. 13–19, 2009.
- [39] S. Hachuda, S. Otsuka, S. Kita, T. Isono, M. Narimatsu, K. Watanabe, Y. Goshima, and T. Baba, “Selective detection of sub-atto-molar streptavidin in 1013-fold impure sample using photonic crystal nanolaser sensor,” *Opt. Exp.*, vol. 21, no. 10, pp. 12815–12821, 2013.
- [40] T.-Y. Chang, M. Huang, A. A. Yanik, H.-Y. Tsai, P. Shi, S. Aksu, M. F. Yanik, and H. Altug, “Large-scale plasmonic microarrays for label-free high-throughput screening,” *Lab Chip*, vol. 11, pp. 3596–3602, 2011.
- [41] Z. Chen, S. M. Tabakman, A. P. Goodwin, M. G. Kattah, D. Darancioglu, X. R. Wang, G. Y. Zhang, X. L. Li, Z. Liu, P. J. Utz, K. L. Jiang, S. S. Fan, and H. J. Dai, “Protein microarrays with carbon nanotubes as multicolor Raman labels,” *Nat. Biotechnol.*, vol. 26, pp. 1285–1292, 2008.

**Yi Zou** received the M.S. degree in electrical and computer engineering from the University of Alabama, Huntsville, AL, USA, in 2010. He is currently working toward the Ph.D. degree in the Department of Electrical and Computer Engineering, the University of Texas, Austin, TX, USA.

His research interests include silicon photonics, photonic sensor, mid infrared photonics, and fiber optics.

**Swapnajit Chakravarty** received the B.E. degree in electrical engineering in 2001 from Jadavpur University, Kolkata, India, the M.S. degree in electrical engineering (Electronic Materials and Devices) from the University of Cincinnati, Cincinnati, OH, USA, in 2003 and the Ph.D. degree in electrical engineering from the University of Michigan, Ann Arbor, MI, USA, in 2007. Dr. Chakravarty has been an active researcher in photonic crystal microcavity devices for the past 10 years. His research area includes electrically and optically injected photonic crystal lasers and light emitting arrays, nanophotonic interconnects and photonic crystal sensors. His current research focuses on utilizing III-V and silicon photonic crystal waveguide devices and photonic crystal microcavity devices for chip-integrated optical sensing and spectroscopy with applications in water and air pollution monitoring, early cancer detection and the detection of various pathogens. Dr. Chakravarty has seven issued patents and over 60 publications in refereed journals and conferences. In 2013, Dr. Chakravarty was elected as Senior Member of IEEE and Senior Member of SPIE.

**David N. Kwong** received the B.S., M.S., and Ph.D. degrees in electrical engineering from the University of Texas, Austin, TX, USA, in 2006, 2010, and 2013 respectively. His research interests include silicon nanophotonic devices for optical interconnects and optical phased arrays.

**Wei-Cheng Lai** received the B.S. and M.S. degrees in physics and photonics and optoelectronics from National Taiwan University, Taipei, in 2007 and 2009, respectively, and the Ph.D. degree from the University of Texas, Austin, TX, USA, in 2013. His research interests include silicon photonics, and photonic crystal sensors.

**Xiaochuan Xu** received the B.Sc. and M.S. degrees in electrical engineering from the Harbin Institute of Technology, Harbin, China, in 2006 and 2009, respectively, and the Ph.D. degree in electrical and computer engineering from the University of Texas, Austin, TX, USA, in 2013.

His research interests include flexible photonics, nonlinear optics, fiber optics, and silicon photonics.

**Xiaohui Lin** received the B.S. and Ph.D. degrees in mechanical engineering from the Huazhong University of Science and Technology, Wuhan, China, in 2004 and 2008, respectively. He also received the Ph.D. degree in electrical and computer engineering from the University of Texas, Austin, TX, USA, in 2013.

His research interests include MEMS and polymer based nanophotonic devices for optical interconnects.

**Amir Hosseini** (S’05–M’13) received the B.Sc. degree in electrical engineering from the Sharif University of Technology, Tehran, Iran, in 2005, M.Sc. degree in electrical and computer engineering from Rice University, Houston, TX, in 2007, and the Ph.D. degree in electrical and computer engineering from the University of Texas, Austin, TX, USA, in 2011.

He is currently working as a Research Scientist at Omega Optics Inc. His research interests include modeling, design, fabrication, and characterization of optical-phased array technology, true-time delay lines, and high performance optical modulators.

Dr. Hosseini was a Prince of Wales’ scholar in 2011, and received the Ben Streetman Award in 2012, and has authored or coauthored more than 70 peer reviewed technical papers. He is the member of the OSA and SPIE. He has been the Principal Investigator for an AFRL sponsored project on polymer optical modulators since 2012.

**Ray T. Chen** (F’04) received the B.S. degree in physics from National TsingHua University, Taiwan, in 1980, the M.S. degree in physics from the University of California, San Diego, CA, USA, in 1983, and the Ph.D. degree in electrical engineering from the University of California, Irvine, CA, USA, in 1988.

He worked as a Research Scientist, a Manager, and the Director of the Department of Electrooptic Engineering in Physical Optics Corporation, Torrance, CA, USA, from 1988 to 1992. He joined the University of Texas (UT), Austin, as a Faculty Member to start optical interconnect research program in the Department of Electrical and Computer Engineering in 1992. He holds the Cullen Trust for Higher Education Endowed Professorship at UT and the Director of Nanophotonics and Optical Interconnects Research Laboratory, Microelectronics Research Center. He is also the Director of a newly formed AFOSR Multidisciplinary Research Initiative Center for Silicon Nanomembrane involving faculty from Stanford, UIUC, Rutgers, and UT. He also served as the CTO/founder and the Chairman of the Board of Radiant Research from 2000 to 2001 where he raised 18 million dollars A-Round funding to commercialize polymer-based photonic devices involving more than 20 patents, which was acquired by Finisar in silicon valley. He also serves as the founder and the Chairman of the Board of Omega Optics, Inc., since its initiation in 2001. More than five million dollars of research funds were raised for Omega Optics. His research work has been awarded with 101 research grants and contracts from sponsors such as DOD, NSF, DOE, NASA, EPA, NIH, the State of Texas, and private industry. There are 35 students who have received the EE Ph.D. degree from his research group at UT, Austin. His group has reported its research findings in more than 560 published papers including more than 70 invited papers. He holds 20 issued patents. His research topics are focused on nanophotonic passive and active devices for optical phased array and interconnect applications, thin film guided-wave optical interconnection and packaging for 2-D and 3-D laser beam routing and steering, and true time delay wide band phased array antenna. In his undergraduate years in National Tsing-Hua University, he led a university debate team in 1979 which received the National Championship of National Debate Contest in Taiwan.

Dr. Chen has chaired or been a program committee member for more than 100 domestic and international conferences organized by the IEEE, the SPIE, the OSA, and the PSC. He has served as an Editor or Coeditor for 18 conference proceedings. He has also served as a Consultant for various federal agencies and private companies and delivered numerous invited talks to professional societies. He received the 1987 UC Regent’s Dissertation Fellowship and of the 1999 UT Engineering Foundation Faculty Award for his contributions in research, teaching, and services. He received the 2008 IEEE Teaching Award and of the 2010 Best Research Professor Award from the IEEE and HKN Honor Society. He is a Fellow of the OSA and the SPIE.